Drug Design, Development and Therapy

Dovepress
Taylor & Francis Group

Open Access Full Text Article

ORIGINAL RESEARCH

Mechanistic Insights into Shenzhuo Formula for Diabetic Retinopathy: Integrating UPLC-Q-TOF-MS/MS, Network Pharmacology, Single-Cell RNA Sequencing Data, and Experimental Validation

Xiaoyu Zang[1,*], Lili Zhang[2,*], Jing Ma[1,3,*], Anzhu Wang[4,*], Lu Ding[1,3,5], Yayun Wang[1], Jun Sun[1], Jing Li[1,5], Xing Hang[6], Xiangyan Li[1,5], Linhua Zhao[2]

[1]Changchun University of Chinese Medicine, Changchun, People's Republic of China; [2]Institute of Metabolic Diseases, Guang' Anmen Hospital, China Academy of Chinese Medical Sciences, Beijing, People's Republic of China; [3]The Affiliated Hospital of Changchun University of Chinese Medicine, Changchun, People's Republic of China; [4]National Center for Integrative Medicine, China-Japan Friendship Hospital, Beijing, People's Republic of China; [5]Northeast Asia Research Institute of Traditional Chinese Medicine, Key Laboratory of Active Substances and Biological Mechanisms of Ginseng Efficacy, Ministry of Education, Jilin Provincial Key Laboratory of Bio-Macromolecules of Chinese Medicine, Changchun, People's Republic of China; [6]Beijing University of Chinese Medicine, Beijing, People's Republic of China

*These authors contributed equally to this work

Correspondence: Linhua Zhao; Xiangyan Li, Email melonzhao@163.com; xiangyan_li1981@163.com

Purpose: For early-stage Diabetic retinopathy (DR), various pharmacological agents and neuroprotective factors have been developed. However, these treatments often show limited efficacy, especially when initiated after retinal damage, and may cause adverse effects. Therefore, there is an urgent need to develop safer and more effective therapeutic strategies for early-stage DR. Shenzhuo Formula (SZF), a modified classical traditional Chinese medicine prescription, has shown promising clinical efficacy in early-stage DR treatment. This study aims to investigate the underlying mechanisms of SZF to expand treatment strategies for DR.

Methods: SZF components were analyzed using Ultra Performance Liquid Chromatography-Quadrupole Time-of-Flight Mass Spectrometry/Mass Spectrometry (UPLC-Q-TOF-MS/MS). Db/db mice received three different SZF doses for 12 weeks. Physiological parameters, including water and food consumption, body weight, and urine output, were monitored. Blood samples were analyzed for fasting blood glucose and other relevant parameters. Ocular changes were assessed using fundus photography (FP), fundus fluorescein angiography (FFA), optical coherence tomography (OCT) and hematoxylin and eosin (H&E). Network pharmacology analysis (NP) identified potential SZF targets, while immunofluorescence staining evaluated SZF's mechanism in delaying DR progression. The distribution of SZF pharmacological targets in critical DR target cells was analyzed using single-cell data from the GSE245561 dataset. Molecular docking predicted SZF-target interactions.

Results: SZF improved diabetic symptoms, increased retinal thickness, and reducedvascular leakage and microcirculation issues. The HIF-1α-VEGFA axis was suggested as a potential core target. Single-cell analysis of clinical samples suggested macrophages as a common target cell for HIF-1α and VEGFA. Molecular docking identified effective SZF components.

Conclusion: Results indicate that SZF may impede the progression of DR by inhibiting the HIF-1α-VEGFA signaling pathway in macrophages, with quercetin and apigenin identified as significant contributors, though further experimental validation is needed to confirm these mechanistic.

Keywords: diabetic retinopathy, Shenzhuo formula, HIF-1α/VEGFA, macrophage, scRNA-seq

Received: 6 November 2024
Accepted: 3 July 2025
Published: 18 July 2025

Graphical Abstract

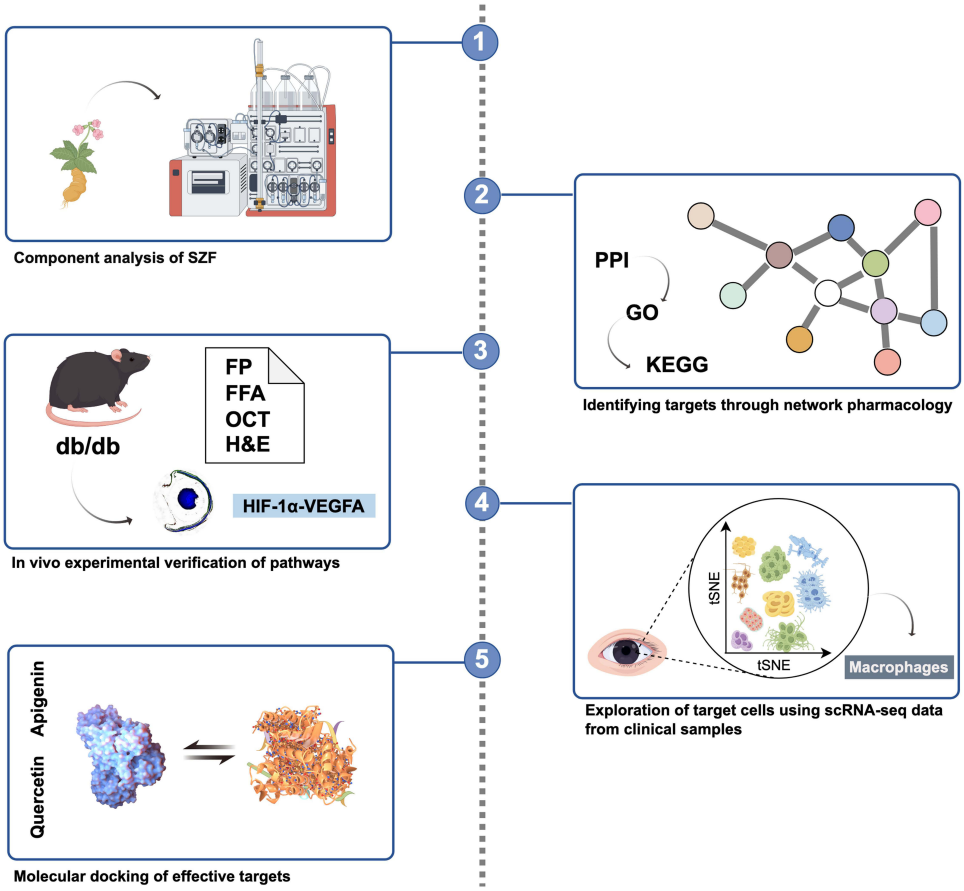

Introduction

The American Diabetes Association (ADA) defines Diabetic retinopathy (DR) as a highly tissue-specific neurovascular complication.[1] Approximately 22.27% of diabetes patients will suffer from DR,[2] making it the fifth largest cause of visual impairment among adults aged 50 and above.[3] DR is characterized by progressive damage to the retinal microvasculature and neurons, involving mechanisms such as oxidative stress, inflammation, and vascular dysfunction.[4] The condition typically progresses from non-proliferative diabetic retinopathy (NPDR) to proliferative diabetic retinopathy (PDR), potentially leading to vision loss.

Current therapeutic strategies for DR include surgical and pharmacological treatments. Surgical approaches such as vitreoretinal surgery and laser photocoagulation are mainly used for advanced proliferative DR with severe complications.[5–7] While anti-VEGF therapy has become a primary treatment option, these interventions are invasive and may cause complications including intraocular inflammation, retinal detachment, and elevated intraocular pressure.[8–13] For early-stage DR, various pharmacological agents have been developed, including neuroprotective factors (insulin-like growth factor-1 (IGF-1), pigment epithelium-derived factor (PEDF), somatostatin (SST), pituitary adenylate cyclase-activating polypeptide (PACAP), glucagon-like peptide-1 (GLP-1), brain-derived neurotrophic factor (BDNF), and nerve growth factor (NGF))[14] and other therapeutic compounds (calcium dobesilate, SGLT2 inhibitors, PPAR-α agonists). However, these treatments often show limited efficacy, especially when initiated after retinal damage, and may cause adverse effects.[10,15] Therefore, there is an urgent need to develop safer and more effective therapeutic strategies for DR.[16]

Traditional Chinese medicine (TCM) exhibits significant advantages in addressing early DR. Notably, Professor Tong Xiaolin has developed a refined formulation, Shenzhuo Formula (SZF), based on the traditional Di dang Tang. This innovative formula primarily comprises *Astragalus mongholicus Bunge, Salvia miltiorrhiza Bunge, Rheum officinale Baill, Hirudo, Epimedium sagittatum (Siebold & Zucc). Maxim*, and *Leonurus japonicus Houtt* among other ingredients. It is known for its efficacy in nourishing qi, enhancing blood circulation, and unblocking collaterals, which positions it favorably compared to standard first-line treatments and pharmaceuticals. While earlier literature documented the use of Di dang Tang for treating Type 2 Diabetes Mellitus (T2DM),[17] there is currently no published research on its application in the treatment of DR.

Interestingly, several key components of SZF have been reported to be beneficial for DR.[18–20] *Astragalus membranaceus* and its main components, such as *Astragaloside IV*, may play a role in the treatment of DR by targeting VEGFA, AKT1, and IL-6 and participating in oxidative stress, angiogenesis, and inflammation.[21] Moreover, quercetin from *Astragalus membranaceus* has been shown to prevent DR in rats by inducing heme oxygenase-1 expression,[22] while kaempferol, another component of *Astragalus membranaceus*, exhibits immunomodulatory effects on microglia and macrophages during the progression of DR.[23] *Leonurus japonicus Houtt*, another key ingredient in SZF, contains chlorogenic acid, which alleviates blood-retinal barrier (BRB) injury by reducing microglia-induced inflammation.[24–26] Furthermore, hyperoside from *Epimedium sagittatum (Siebold & Zucc). Maxim* has been found to reduce oxidative stress and inhibit cell damage,[27] suggesting its potential role in DR treatment. These findings collectively highlight the therapeutic potential of SZF and its individual components in the management of DR. The synergistic effects of these ingredients may contribute to the overall efficacy of SZF in treating this complex condition.

This study aims to: (1) evaluate the therapeutic efficacy of SZF in DR treatment; (2) identify the key active compounds and their molecular targets; (3) elucidate the underlying mechanisms through which SZF exerts its protective effects on retinal vessels and neurons.

Materials and Methods

Ultra Performance Liquid Chromatography-Quadrupole Time-of-Flight Mass Spectrometry/Mass Spectrometry (UPLC-Q-TOF-MS/MS) Analysis

Preparation of Standard and Sample Solutions

A total of twenty-nine standard substances were utilized in this study. These include: Astragaloside III (DST181118-018), Astragaloside II (DST180315-023), Isoastragaloside II (DST180315-023), Astragaloside I (DST190216-016), Isoastragaloside IV (ST81100105), (6aR, 11aR)-3-hydroxy-9,10-dimethoxy pterocarpan-7-O-β-D-glucoside (ST19060210), Astraisoflavan-7-O-β-D-glucoside (ST80460105), complanatuside (ST11380120), Calycosin (ST08810120), Calycosin 7-O-glucoside (ST08820120-5240), Astragalin (ST07310120-3289), Formononetin (ST08800120-1948), Astragaloside A (DST190711-015), and Genistin (ST02430120). All these compounds were procured from Chengdu Dest Biotechnology Co., Ltd. Additionally, the following substances were included: Emodin (5940), Emodin-3-methyl ether (7550), Aloe emodin (8075), Aloe-emodin-8-O-β-D-glucopyranoside (5421), lithospermic acid (ST13620120MG), Dihydrotanshinone I, and Salvianolic acid (ST005570120MG-4881), along with Salvianolic acid C and Cryptotanshinone (110852–200,806), 2-Propenoic acid, 3-[2-[(1E)-2-(3,4-dihydroxyphenyl)ethenyl]-3,4-dihydroxyphenyl]- (2E) (DST180404-075), lithospermic acid B (ST000500120MG-4065), Danshensu, and Ferulic acid (110773–201,012), as well as Protocatechualdehyde (110810–201007) and Rosmarinic acid (DST190506-027). To prepare a mixed standard solution, an appropriate volume of methanol was added to dissolve 1.00 mg of each reference substance, followed by dilution to a concentration of 50 μg/mL.

For fingerprint analysis and similarity evaluation, SZF granules (20 mg) were accurately weighed and dissolved in 1 mL of ultrapure water by vortexing and sonication to prepare a solution with a concentration of 20 mg/mL. The solution was centrifuged at 14,000 rpm for 10 min at 4°C, and the supernatant was collected and stored for later use. For chemical component identification, 20 mg of SZF formula solution was accurately measured and dissolved in 1 mL of ultrapure water by vortexing to prepare a 5 mg/mL SZF solution, which was then centrifuged, and the supernatant was collected. Single herb sample solutions were prepared by weighing 10 g of each herb, soaking them in 8 times the volume of water for 30 minutes, and heating the mixture under reflux for 1 hour. After cooling and adjusting for any weight loss, the solution was filtered, and 1 mL of the filtrate was diluted to a concentration of 5 mg/mL, centrifuged, and the supernatant was collected.

UPLC-Q-TOF-MS/MS Conditions

UPLC-Q-TOF-MS/MS analysis was performed for fingerprint analysis, similarity evaluation, and chemical component identification of SZF. Chromatographic separation was achieved using a Phenomenex Kinetex XB-C18 column (2.1 x 100 mm, 2.6 μm) at 35°C for fingerprint analysis and a Waters Acquity UPLC BEH C18 column (2.1 x 100 mm, 1.7 μm) at 30°C for component identification. The mobile phases consisted of (A) 0.1% phosphoric acid or formic acid and (B) 0.1% phosphoric acid or formic acid in acetonitrile, with gradient elution programs ranging from 0–38 min and 0–42 min, respectively. The flow rates were 0.7 mL/min and 0.3 mL/min, with injection volumes of 5 μL (SZF) and 2 μL (standards). Mass spectrometric detection was performed using the HDMS^E acquisition method in both positive and negative ionization modes. The ESI parameters were set as follows: capillary voltage 2.5 kV, cone voltage 60 V, source temperature 120°C, desolvation temperature 500°C, cone gas (N_2) flow 50 L/h, and desolvation gas (N_2) flow 800 L/h. The collision energy was 6 eV (low) and 20–50 eV (ramp), with a mass range of m/z 100–1500. Data processing was conducted using UNIFI^{TM} 1.9.3.0 software for HDMS^E data correction and automatic peak annotation with an in-house database. Key parameters included peak finding intensity thresholds, mass deviation, isotope selection, fragment matching, adduct ions, and lock mass settings for both negative and positive modes.

Data and Methods of Network Pharmacology

SZF Active Ingredients and Disease Target Prediction

The obtained ingredients were inputted into the SwissTarget Prediction database (http://www.swisstargetprediction.ch/) to identify their potential targets of action. A table was organized to display the results according to the following structure: "Traditional Chinese Medicine - Ingredient Code - Ingredient Name - Target". Furthermore, the GeneCards database (https://www.genecards.org/) was utilized to gather data on disease targets specifically related to the keyword "diabetic retinopathy". This systematic approach enables a comprehensive understanding of the connections between the identified ingredients and their potential therapeutic roles in the context of DR.

Building a Traditional Chinese Medicine Compound Regulation Network

The potential targets identified for SZF were analyzed to find their intersections with relevant genes, and a Venn diagram was created utilizing R packages to visually represent this overlap. Subsequently, a regulatory network for the traditional Chinese medicine compounds was constructed using Cytoscape version 3.8.2, where the intersecting genes and active ingredients served as nodes within the network. This approach facilitates a better understanding of the interactions between the compounds and their target genes, highlighting the intricate relationships that underpin the therapeutic effects of traditional Chinese medicine.

Construction of PPI Protein Interaction Network and Screening of Hub Genes

The STRING database (https://www.string-db.org/) serves as a resource for constructing a protein-protein interaction (PPI) network using commonly identified differentially expressed genes.[28] Nodes within the network that are not related and possess a confidence score below 0.4 are filtered out to enhance clarity. For visualization purposes, Cytoscape 3.8.2 software is utilized, while the CytoHubba plugin facilitates the identification of the top 10 hub targets based on node scores.[29] Additionally, the MCODE plugin[30] is employed to pinpoint key modules within the PPI network, applying the following criteria for screening: degree cutoff set at 2, node score cutoff at 0.2, K-score at 2, and a maximum depth of 100. The module achieving the highest score is regarded as the final functional module. The intersection of the hub targets and the key modules identified by MCODE represents the core targets of the PPI network. To deepen the understanding of the biological characteristics associated with these core targets, the GeneMANIA platform is leveraged to construct and analyze a network comprising the core genes and their co-expressed counterparts.[31]

Functional Enrichment Analysis

Gene Ontology (GO) provides functional annotations for genes, enabling the understanding of their biological roles. On the other hand, the Kyoto Encyclopedia of Genes and Genomes (KEGG) is utilized to analyze and map various signaling pathways associated with these genes. For the purposes of visualization, R packages are employed to create informative and insightful graphical representations of this data.[32]

Analysis of Single-Cell RNA Sequencing Data and Identification of DR Related Genes

The single-cell RNA sequencing data (accession number: GSE245561) was downloaded from the Gene Expression Omnibus (GEO) database. Four preterminal fibrous membrane samples were selected for downstream analysis. Quality control and data preprocessing were performed using Seurat package (version 4.0.0) in R software (version 4.2.0). The following filtering criteria were applied: cells expressing fewer than 3 genes were removed (min.cells=3); genes detected in fewer than 200 cells were filtered out (min.features=200); cells with total feature counts between 300 and 10,000 were retained ($nFeature_RNA $\geq$ 300 and $\leq$ 10,000); cells with mitochondrial gene percentage > 10% were excluded ($percent.mt $\leq$ 10); and cells with ribosomal gene percentage > 1% were removed ($percent.rb $\leq$ 1).

After quality control, data normalization was performed using the LogNormalize method with a scale factor of 10,000. The top 2000 highly variable genes were identified using the "FindVariableFeatures" function with "vst" method. Principal component analysis (PCA) was performed on the scaled data, and the first 30 principal components were selected based on elbow plot visualization. For dimensionality reduction and visualization, t-distributed stochastic neighbor embedding (t-SNE) analysis was performed on the PCA-reduced data. Cell clustering was performed using the shared nearest neighbor (SNN) modularity optimization with a resolution parameter of 0.9, resulting in 20 distinct clusters.

Cell type annotation was performed based on the expression of canonical marker genes: PDGFRB and ACTA2 for Pericytes; CD68 and CD163 for Macrophages; ACTA2 and COL1A1 for Myofibroblasts; PECAM1 and VWF for Endothelial cells; CD8A and CD3D for CD8+ T Cells; NCAM1 and KLRD1 for Natural Killer Cells; CD1C and CLEC10A for Dendritic Cells; and CD19 and CD79A for B Cells. Differentially expressed genes (DEGs) were identified using the "FindAllMarkers" function with Wilcoxon rank sum test (adjusted p-value < 0.05, $|log2FC| > 0.25$).

The expression patterns of HIF1A and VEGFA were analyzed across different cell populations. Feature plots and violin plots were generated to visualize their cell-type specific expression patterns.

Experimental Verification

Animal Studies and Drug Intervention

C57BL/KsJdb/db mice serve as a well-established spontaneous model for studying type 2 diabetes, while their non-diabetic counterparts, the db/m mice, provide a crucial control group for comparative analyses. In this study, a total of 40 male db/db mice and 10 male db/m mice were utilized, all of which were 7 weeks old at the time of experimentation. These mice were obtained from Changzhou Kavins Experimental Animal Co., Ltd., which holds the animal license number SCXK (Su) 2021–0013. The housing conditions for the mice were strictly maintained under specific pathogen-free (SPF) standards, ensuring a controlled environment that minimizes the risk of infections and other confounding factors. The mice were provided with a standard diet that is essential for their growth and maintenance. Temperature control was set within a range of 22 to 25 °C, while the relative humidity was carefully regulated at 55 ± 5%, creating an optimal living environment for the animals. Additionally, the light/dark cycle was systematically arranged to provide 12 hours of light followed by 12 hours of darkness, simulating natural conditions (with the light period set from 7:00 to 19:00). The diet administered to the mice was procured from Jiangsu Xietong Biotechnology Company and was formulated to include 22.8% protein, 13.8% fat, and 63.4% carbohydrates, ensuring that the dietary needs of the growing mice were adequately met. Furthermore, the mice were allowed unrestricted access to both food and fresh water, promoting healthy feeding behaviors. Ethical considerations for the treatment of these animals were paramount; hence, all experimental procedures were meticulously reviewed and approved by the Experimental Animal Ethics Committee of Changchun University of Traditional Chinese Medicine. This study was approved by the Experimental Animal Ethics Committee of Changchun University of Traditional Chinese Medicine (approval number: 2024743) and followed the "Guiding Opinions on Treating Experimental Animals with Kindness" (2006) and "Guidelines for the Ethical Review of Laboratory Animal Welfare" (2020) issued by China's Ministry of Science and Technology. All animal experiments were designed to minimize pain and discomfort.

Following one week of adaptive feeding in animal models, fasting blood glucose levels were assessed at the tail tip of mice. Results indicated that the blood glucose concentrations in the db/db group were significantly elevated compared to the db/m group. The mice were categorized into five distinct groups based on their blood glucose levels and body weights: the normal group (db/m), model group (db/db), low-dose group, medium-dose group, and high-dose group.

According to the established daily protocol, the SZF decoction pieces were immersed in distilled water for 30 minutes and then decocted twice. The first decoction yielded 500 mL and the second produced 300 mL, with each decoction lasting 30 minutes. After filtration, the two decoctions were combined, freeze-dried, and stored at 4 °C, resulting in a total of 16.2975 g per dose of the medication. This dosage was determined based on the equivalent dose of SZF reported in two large-scale clinical studies by Chen 2017 and Zhao 2018.[33,34]

For a typical adult weighing 70 kg, the SZF is administered once daily at a dosage of 16.2975 g. The dosing conversion for mice, based on body surface area, follows the methodology outlined in Professor Xu Shuyun's book, "Pharmacological Experimental Methodology"[35]: equivalent dose for mice (mg/kg) = 9.1 * clinical dose for humans (mg/kg). Consequently, the medium-dose group received a daily oral gavage of 2.11868 mg/g/d, which corresponds to the human equivalent dose. The low-dose and high-dose groups were given 1.05934 mg/g/d and 4.23736 mg/g/d, respectively, which are 0.5 and 2 times the equivalent dose.

Prior to the formal experiment, we conducted preliminary experiments using these three doses and observed no obvious toxic reactions in the mice. For the 12-week treatment period, the low, medium, and high-dose groups received SZF solution via gavage once daily at their respective doses. The SZF solution was prepared by diluting the freeze-dried powder with sterile water for oral administration. During this period, both db/m and db/db mice in the normal and model groups were given equal volumes of sterile water via gavage.

Feeding and water intake for each cage, containing five mice, were monitored every six days, and average values were calculated. Body weight was assessed once a month, and urine output was collected over a 12-hour period using metabolic cages. Prior to this, the mice were euthanized after fasting overnight. Subsequently, fasting serum samples were obtained for analysis. Using a fully automated biochemical analyzer (Mindray BS-240VT), serum levels of GLU, ALT, AST, CREA, UREA, and BUN/CREA were measured.

Fundus Photography and Fluorescein Fundus Angiography (FP and FFA)

Morphological and pathological alterations in the fundus of db/db mice were examined using a Micron IV retinal imaging microscope. Continuous anesthesia was maintained using isoflurane, and pupil dilation was achieved with a compound tropicamide eye drop solution (0.5%; 0.05 mL). Each mouse was positioned on the microscope platform, and OmniVision (SA, Neuhausen, Switzerland) was applied to their eyes. Following the color FP, FFA was performed through an intraperitoneal injection of fluorescein sodium solution (10%; 0.05 mL).

Optical Coherence Tomography (OCT) Imaging and Retinal Thickness Analysis

The OCT module integrated into the Micron IV retinal imaging microscope was employed to obtain high-resolution images that reveal the intricate structures of various retinal layers. This study specifically utilized the InSight 2D software for the segmentation of the entire visual field of the retina, enabling a comprehensive analysis through hierarchical statistical methods. The focus was placed on measuring three distinct layers of the retina: the Ganglion Cell Layer (GCL), which is crucial for transmitting visual information; the Inner Nuclear Layer (INL), which contains the cell bodies of several types of neurons; and the Outer Nuclear Layer (ONL), where the photoreceptor cell bodies reside. Additionally, the total retinal thickness was assessed to provide further insights into the overall structural integrity of the retina.

H&E Staining

Following euthanasia, eyes were carefully enucleated and immediately fixed in 4% paraformaldehyde at 4°C for 24 hours. The fixed tissues were processed through graded ethanol series for dehydration, cleared in xylene, and embedded in paraffin. Paraffin sections (4 μm thickness) were cut and mounted on glass slides. For histological analysis, sections were stained with hematoxylin and eosin (H&E) following standard protocols. The stained sections were examined under a light microscope to assess retinal structure and measure layer thickness.

Regional Blood Flow Velocity and Perfused Blood Vessel Area Detection

Mice were anesthetized with isoflurane. Regional blood flow velocity and perfused blood vessel area of plantar skin were measured using a Laser Speckle Imaging System (RFLSI III, RWD). Relative perfusion volume was quantified using the mean value of the region of interest (ROI).

Immunofluorescence

Paraffin sections were dried for 1 h followed by antigen retrieval for 1 h. The sections were washed three times with PBS (pH 7.4) for 5 min each on a shaker. After removing excess moisture, sections were incubated with 3% hydrogen peroxide solution for 25 min at room temperature in darkness, followed by three 5-min PBS washes.

Sections were blocked with a mixture of 10% goat serum and 3% BSA in a humid chamber for 30 min at room temperature. After removing the blocking solution, primary antibodies were diluted in sterile PBS: VEGFA (Abcam, ab52917, 1:100) and HIF-1α (Proteintech, 20960-1-ap, 1:50). Sections were incubated with primary antibodies overnight at 4°C in a dark, humid chamber.

Following overnight incubation, sections were washed three times with PBS for 5 min each. HRP-conjugated secondary antibodies were applied and incubated for 50 min at room temperature in darkness. After three 5-min PBS washes, TSA reagents were added: VEGFA-iF488 Tyramide (Servicebio, G1231, 1:500) and HIF-1α-iF647 Tyramide (Servicebio, G1232, 1:500). Sections were incubated for 10 min at room temperature in darkness, followed by three 5-min TBST washes.

Nuclei were counterstained with DAPI for 10 min at room temperature in darkness, followed by three 5-min PBS washes. Auto-fluorescence quencher was applied for 5 min, followed by three 5-min PBS washes. Sections were mounted with anti-fade mounting medium. Images were acquired using CaseViewer software.

Molecular Docking

Molecular docking analyses were performed to investigate the binding interactions between active compounds of SZF and key target proteins (HIF1A and VEGFA) identified from the PPI network analysis. The three-dimensional crystal structures of target proteins were obtained from the RCSB Protein Data Bank (https://www.rcsb.org/). Prior to docking, the protein structures were preprocessed using PyMOL software (version 2.5) by removing water molecules, adding hydrogen atoms, and extracting co-crystallized ligands. The 3D structures of the compounds were obtained from the PubChem database and optimized using energy minimization.

The docking analyses were performed using both AutoDock Vina (version 1.1.2) and CB-dock2, with 5 independent docking runs for each analysis.[36] For AutoDock Vina, the grid box was centered on the active site of each protein with dimensions sufficient to encompass all potential binding sites. The binding poses were visualized and analyzed using PyMOL to identify key protein-ligand interactions, including hydrogen bonds, van der Waals interactions, and π-alkyl interactions. For each complex, the binding site residues and interaction types were mapped and presented in 2D interaction diagrams. The molecular surface representation, detailed binding pose analysis, and protein-ligand interaction maps were generated to visualize the binding modes between compounds and target proteins.

The evaluation of molecular docking results was performed using binding energy thresholds based on literature. Referring to studies by Reda and Platania on HIF-1α and VEGFA inhibitors,[37,38] we defined binding energies below −7.5 kcal/mol as strong binding, between −7.5 and −6.5 kcal/mol as moderate binding, and above −6.5 kcal/mol as weak binding. These thresholds were established based on the reported binding energies of the HIF-1α positive control inhibitor 2-methoxyestradiol (2-ME2, −6.68 kcal/mol) and the VEGFA inhibitor ranibizumab (−7.0 kcal/mol).

Statistical Analysis

The statistical analysis was performed using GraphPad Prism 9.0. The normality of data distribution was assessed using the Shapiro–Wilk test, supplemented with Q-Q plots for visual assessment of normality due to the small sample size ($n \geq 5$ per group; see Figure S1). Homogeneity of variance was verified using the Brown-Forsythe test. Data are presented as mean ± standard error (SE) for normally distributed data. The sample size was determined based on previously published similar studies in diabetic retinopathy models and ethical considerations to minimize animal use following the 3Rs principle (Replacement, Reduction, and Refinement).[39] Additionally, sample size adequacy was confirmed using the Resource Equation Method (REM).[40] Our study included 5 experimental groups with n=5 mice per group, and the error degrees of freedom (E) was calculated as E=Total N-Number of groups=25-5=20 for primary biochemical analyses, falling within the REM-recommended range of 10–20. For OCT retinal measurements and serum biomarker analyses, we used slightly larger sample sizes (n=6-8) due to measurement variability, resulting in E values of 25–35. While these

values slightly exceed conventional recommendations, this approach ensures statistical rigor for technically challenging measurements while maintaining ethical standards. Each experimental group contained n=5-8 independent biological replicates (individual animals), with each animal contributing one data point per analysis, maintaining statistical independence for conventional parametric analyses. For multiple group comparisons, conventional one-way analysis of variance (ANOVA) was used when variances were homogeneous, followed by Tukey's HSD test for post hoc pairwise comparisons. For data that did not follow normal distribution, Kruskal–Wallis test was used for multiple group comparisons, followed by Dunn's multiple comparisons test for post hoc analysis. When the Brown-Forsythe test indicated unequal variances, Welch's ANOVA was applied instead, followed by Games-Howell test for post hoc pairwise comparisons. All post hoc tests included appropriate correction for multiple testing to control family-wise error rate. A p-value < 0.05 was considered statistically significant.

Results

Chemical Components of SZF Extract and Quality Control

UPLC-Q-TOF-MS/MS analysis was performed to characterize the chemical composition of SZF and evaluate batch-to-batch consistency. The extraction ion chromatograms of all identified compounds in the formula are shown in Figure 1A and B. Among 152 identified compounds, 29 were validated using reference standards. Each compound was traced to specific herbs in the formula, including Astragalus, Rhubarb, and Salvia miltiorrhiza. The identified compounds encompassed a diverse chemical profile, including cryptotanshinone, danshensu, protocatechualdehyde, ferulic acid, Aloe-eModin-8-O-β-D-glucopyranoside, emodin-3-methyl ether, calycosin 7-O-Glucoside, genistin, lithospermic acid, astragalin, and 2-propenoic acid, 3-[2-[(1E)-2-(3,4-dihydroxyphenyl)ethenyl]-3,4-dihydroxyphenyl]-, (2E)-. A complete list of compounds is provided in Tables S1 and S2. Quality control analysis of twelve SZF batches against a reference spectrum yielded similarity indices ranging from 0.886 to 0.995, demonstrating high batch-to-batch consistency (Figure 1C and D, Table S3). These results confirm the reproducibility of the SZF manufacturing process.

Effects of SZF on Basic Physiological Parameters

At week 12 of SZF administration, db/db mice reached 20 weeks of age, satisfying the criteria for DR model establishment. No signs of toxicity or mortality were observed in any SZF treatment group throughout the study period. After 12 weeks of treatment, mice receiving medium and high doses of SZF showed a trend towards reduced average daily food intake, although the difference was not statistically significant. However, at day 84, low-dose SZF significantly decreased water consumption per mouse (Figure 2A and B). Urine output showed no significant difference between db/db and db/m groups before gavage initiation. However, SZF has little effect on urine output in mice (Figure 2C). Low-dose SZF significantly improved fasting blood glucose levels in db/db mice (Figure 2D) without substantial body weight changes (Figure 2E), suggesting absence of systemic toxicity or growth inhibition. SZF demonstrated high safety profiles, evidenced by effective reduction of AST in the medium-dose group and decreased BUN/CREA ratios across all SZF groups in a dose-dependent manner (Figure 2F and G), indicating no significant hepatic or renal toxicity at therapeutic doses.

SZF Alleviates Retinal Lesions in Db/Db Mice

OCT was employed to evaluate retinal structural changes at week 12 post-gavage. The analysis revealed significantly reduced retinal thickness in db/db mice compared to db/m mice. High-dose SZF treatment effectively restored overall retinal thickness. Specifically, examination of retinal layers (GCL, INL, and ONL) showed marked thinning of the INL and ONL in db/db mice compared to db/m controls. High-dose SZF treatment significantly increased the thickness of these layers, while low and medium doses demonstrated dose-dependent improvements thickness. No additional abnormalities, such as retinal edema, were observed (Figure 3A). H&E staining confirmed that SZF treatment enhanced the thickness of ONL, INL, and GCL in a dose-dependent manner, particularly at medium and high doses. The db/db group exhibited mild ganglion cell loss and disorganization of retinal cellular architecture (Figure 3B). Collectively, OCT and HE staining results suggest that SZF may ameliorate DR primarily through restoration of INL and ONL thickness.

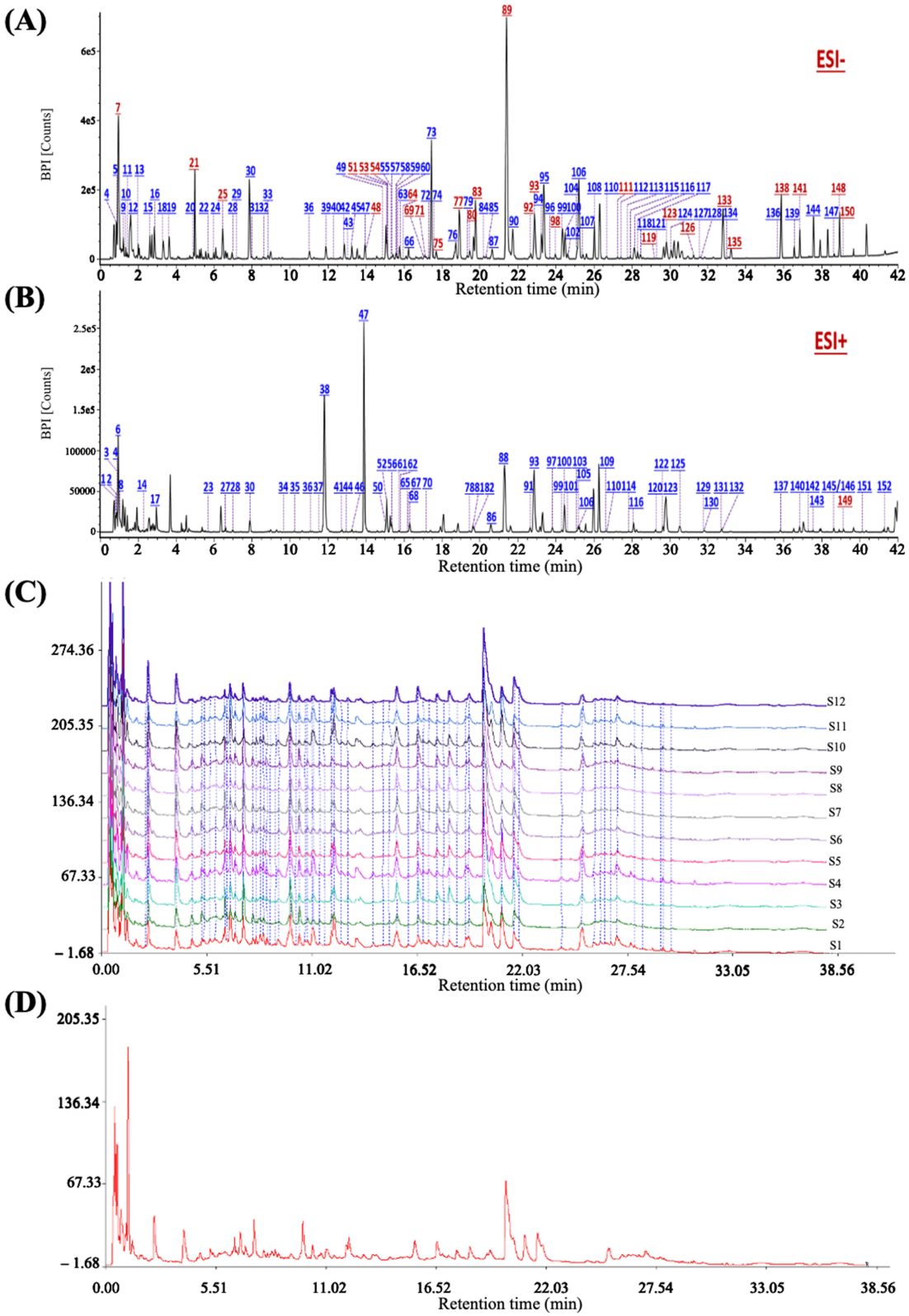

Figure 1 Mass spectrum of SZF. (**A**) Negative ion mode. (**B**) Positive ion mode. Blue numbers indicate the compounds identified based on comparisons with the reference standards. (**C** and **D**) The reproducible HPLC fingerprints of the mixture of 29 standard compounds and 12 batches of QM (S1–S12), using the Chinese Medicine Chromatographic Fingerprint Similarity Evaluation System (2012 Edition).

https://doi.org/10.2147/DDDT.S505055

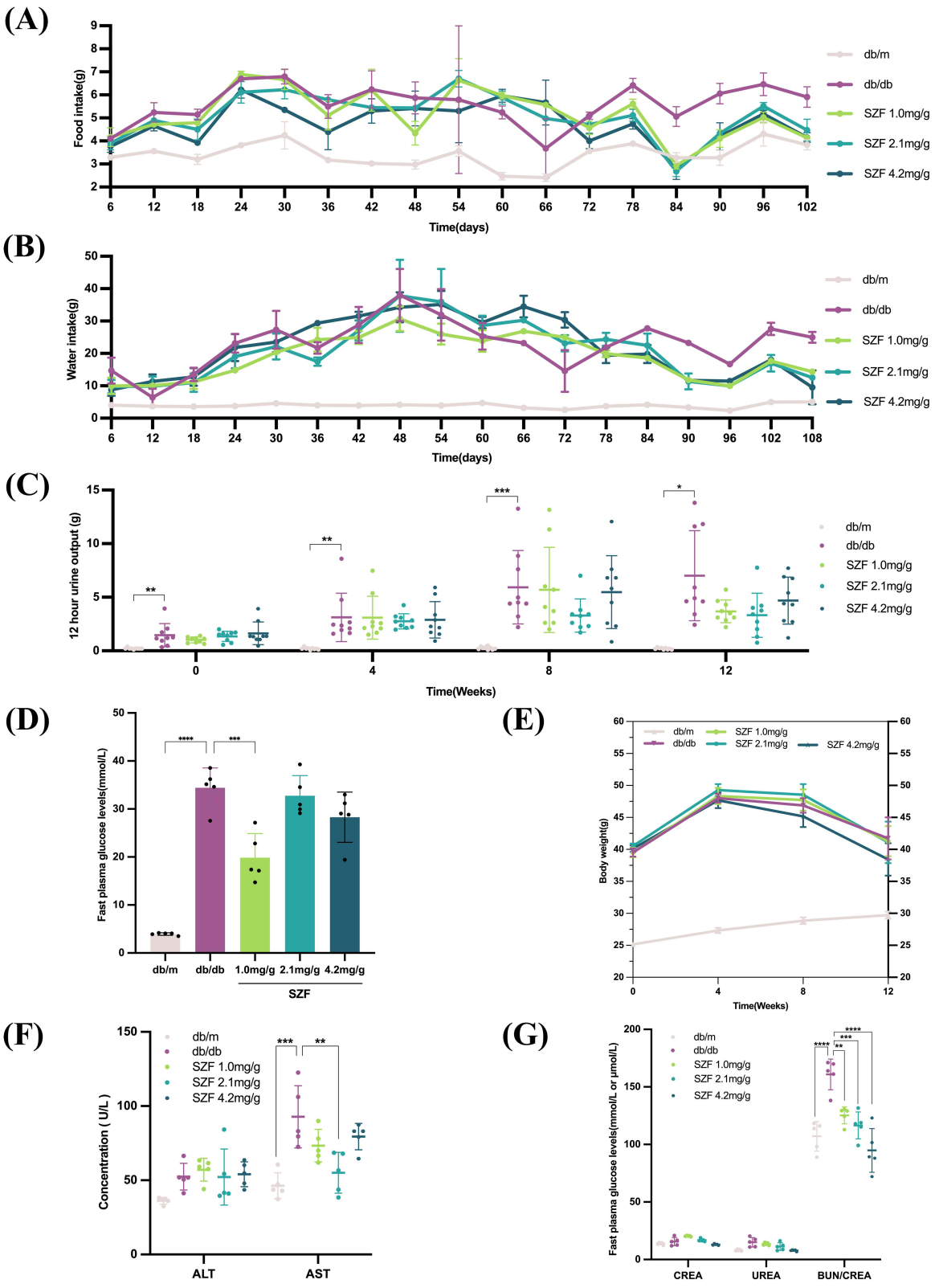

Figure 2 SZF improved the symptoms of diabetes in db/db mice. (**A**) Effect of db/db and db/m on the average daily food intake of each mouse. (**B**) Effect of db/db and db/m on the average daily water intake of each mouse. (**C**) Effect of db/db and db/m on 12 hour urine output. (**D**) Fasting blood glucose levels of db/db and db/m mice. (**E**) Weigh db/db and db/m mice every month. (**F**) Effects of liver function markers (ALT, AST) in experimental mice. (**G**) Kidney function markers (CREA, UREA, BUN/CREA) in experimental mice. *P<0.05, **P<0.01, ***P<0.001, ****P<0.0001.

 https://doi.org/10.2147/DDDT.S505055

FP analysis revealed cotton wool spot-like retinal lesions in db/db mice, characterized by white coloration, indistinct margins, irregular shapes, and cloud-like appearance, suggesting localized retinal microvascular occlusions. These lesions were notably absent prevented by SZF treatment (Figure 4A). FFA examination of vascular abnormalities demonstrated increased vascular leakage in db/db mice compared to db/m controls. SZF treatment substantially reduced this abnormal leakage. No significant vascular dilation or microaneurysms were detected in any group (Figure 4B).

SZF Improves Foot Microcirculation in Db/Db Mice

Foot perfusion was quantitatively assessed using a laser Doppler imaging system. Analysis revealed that db/db mice exhibited significantly reduced foot perfusion compared to the control group. Administration of SZF resulted in a dose-dependent improvement in foot perfusion. Notably, high-dose SZF treatment led to a marked increase in perfusion levels, with statistically significant differences observed (Figure 4C). These findings demonstrate that SZF effectively enhances peripheral microcirculation in diabetic mice.

Target Gene Screening and SZF Regulatory Network Construction

Our previous results demonstrated that SZF effectively delays DR progression in db/db mice. To investigate the underlying mechanisms, we performed a comprehensive network pharmacology analysis. UPLC-Q-TOF-MS/MS-identified compounds from SZF were analyzed using the SwissTarget Prediction database, yielding 655 unique potential targets. Cross-referencing these with 4023 DR-associated targets from the GeneCards database identified 344 shared targets (Figure 5A).

Using Cytoscape 3.8.2, we constructed a compound-target network comprising 395 nodes and 1457 edges. The network analysis highlighted functional interactions between compounds and targets, with highly connected nodes indicating greater biological significance. Five active compounds - Magnoflorine, Apigenin, Isorhamnetin, Quercetin, and Kaempferol - showed particularly high connectivity (Figure 5B).

Protein-protein interaction analysis of the 344 shared targets using STRING generated a network with 18 nodes and 7392 edges (Figure 5C). The CytoHubba plugin identified ten crucial targets: STAT3, GAPDH, BCL2, CASP3, HIF1A, MTOR, CTNNB1, JUN, TNF, and ESR1 (Figure 5D). MCODE clustering analysis revealed 11 functional modules, with the primary module containing these same key targets (Figure 5E).

GeneMANIA analysis generated an extended network of 30 genes (including 20 related genes) with 265 connections. Analysis of the hub genes revealed multiple interaction types: physical interactions (52.34%), co-expression (26.87%), co-localization (6.30%), predicted interactions (5.84%), genetic interactions (4.33%), and pathway involvement (4.31%). These targets were primarily associated with miRNA regulation by RNA polymerase II (Figure 5F).

Functional Enrichment Analysis

GO functional analysis was performed on the 344 shared targets between SZF and DR. This analysis revealed a comprehensive spectrum of biological processes, encompassing 2679 BP categories, 117 CC categories, and 232 MF categories, highlighting the extensive biological implications of these targets (Figure 6A). Subsequent KEGG pathway enrichment analysis identified 180 pathways potentially regulated by these targets (Figure 6B). Additionally, a co-expression network was constructed to visualize the interactions between differentially expressed genes (DEGs, shown as gray nodes) and their associated pathways (represented as yellow nodes), with colored edges indicating the specific pathways engaged by different genes (Figure 6C).

Identifying Target Genes Through Single-Cell RNA Data Analysis

Single-cell RNA sequencing data were obtained from the GEO database for comprehensive analysis. After implementing stringent quality control measures, batch effects were eliminated using the Harmony software package, enabling optimal clustering of the dataset at a resolution of 0.9. The t-distributed stochastic neighbor embedding (t-SNE) dimensionality reduction analysis identified 20 distinct cell clusters (Figure 7A) and revealed characteristic biomarkers within each cluster (Figure 7B). Drawing from established literature, these clusters were categorized into eight cell types: endothelial cells, macrophages, dendritic cells, B cells, natural killer cells, CD8+ T cells, myofibroblasts, and pericytes (Figure 7C).

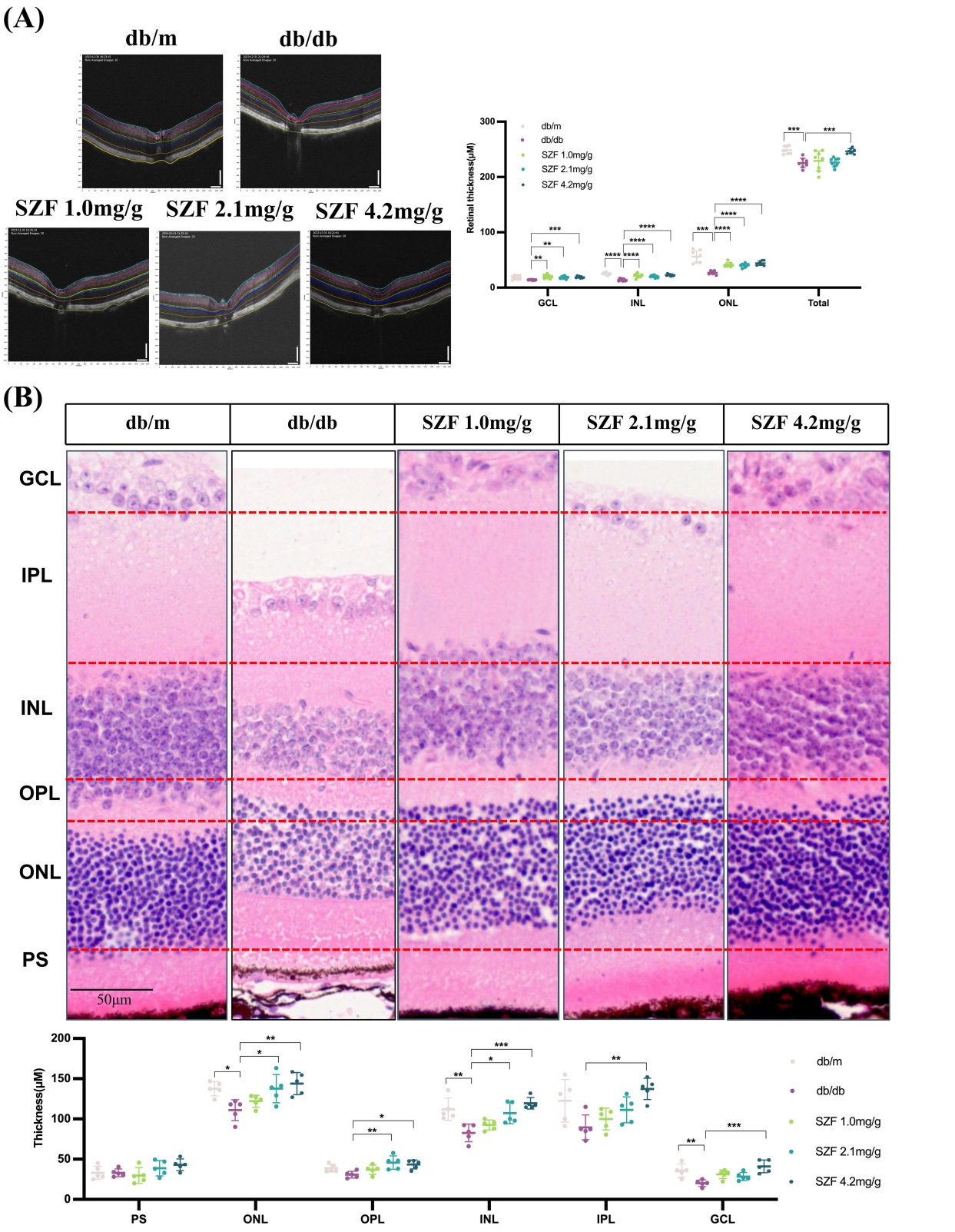

Figure 3 Changes in Retinal Thickness of db/db Mice by SZF. (**A**) Representative images of OCT in five groups of mice retina and quantitative analysis results of GCL, INL, ONL, and total retinal thickness. (**B**) Quantitative analysis of five representative retinal HE staining images and retinal layer thickness, including Ganglion cell layer (GCL), Inner plexiform layer (IPL), Inner nuclear layer (INL), Outer plexiform layer (OPL), Outer nuclear layer (ONL) and Photo receptor segments (PS). Scale bar, 50 μ m. *P<0.05, **P<0.01, ***P<0.001, ****P<0.0001.

 https://doi.org/10.2147/DDDT.S505055

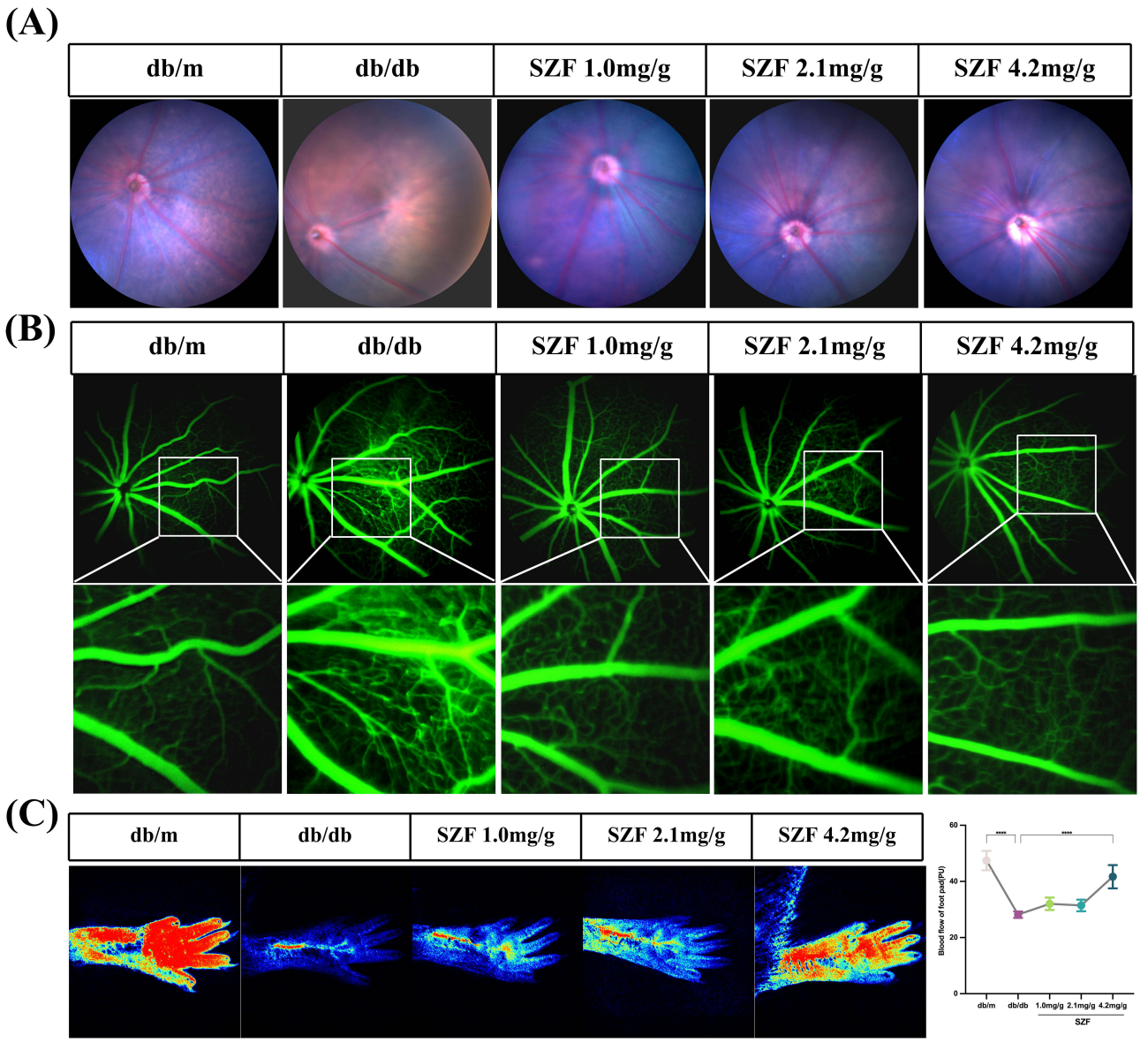

Figure 4 Effect of SZF on retinopathy in diabetic mice. (**A**) FP presented five representative fundus images of mice. (**B**) FFA shows the effect of SZF on retinal vascular lesions in DR mice, and the white box selects the same position to display the enlarged vascular leakage. n=5. (**C**) Quantitative analysis of representative images of plantar perfusion area and blood flow velocity in five groups of mice and their relative perfusion volume calculated using ROI mean. The flow rate and perfusion area are displayed in different colors from low to high, such as blue, green, yellow, orange, and red. ****($P < 0.0001$).

A heatmap was constructed to visualize the distinct gene expression patterns across these clusters (Figure 7D). Furthermore, the expression profiles of HIF1A and VEGFA are presented in Figure 7E–H, respectively.

SZF Reduces Serum Inflammation

The serum levels of TNF-α and STAT3 were quantified using specific ELISA kits. The results revealed that SZF administration significantly reduced these inflammatory markers, as demonstrated by decreased cytokine levels (Figure 8A and B).

https://doi.org/10.2147/DDDT.S505055

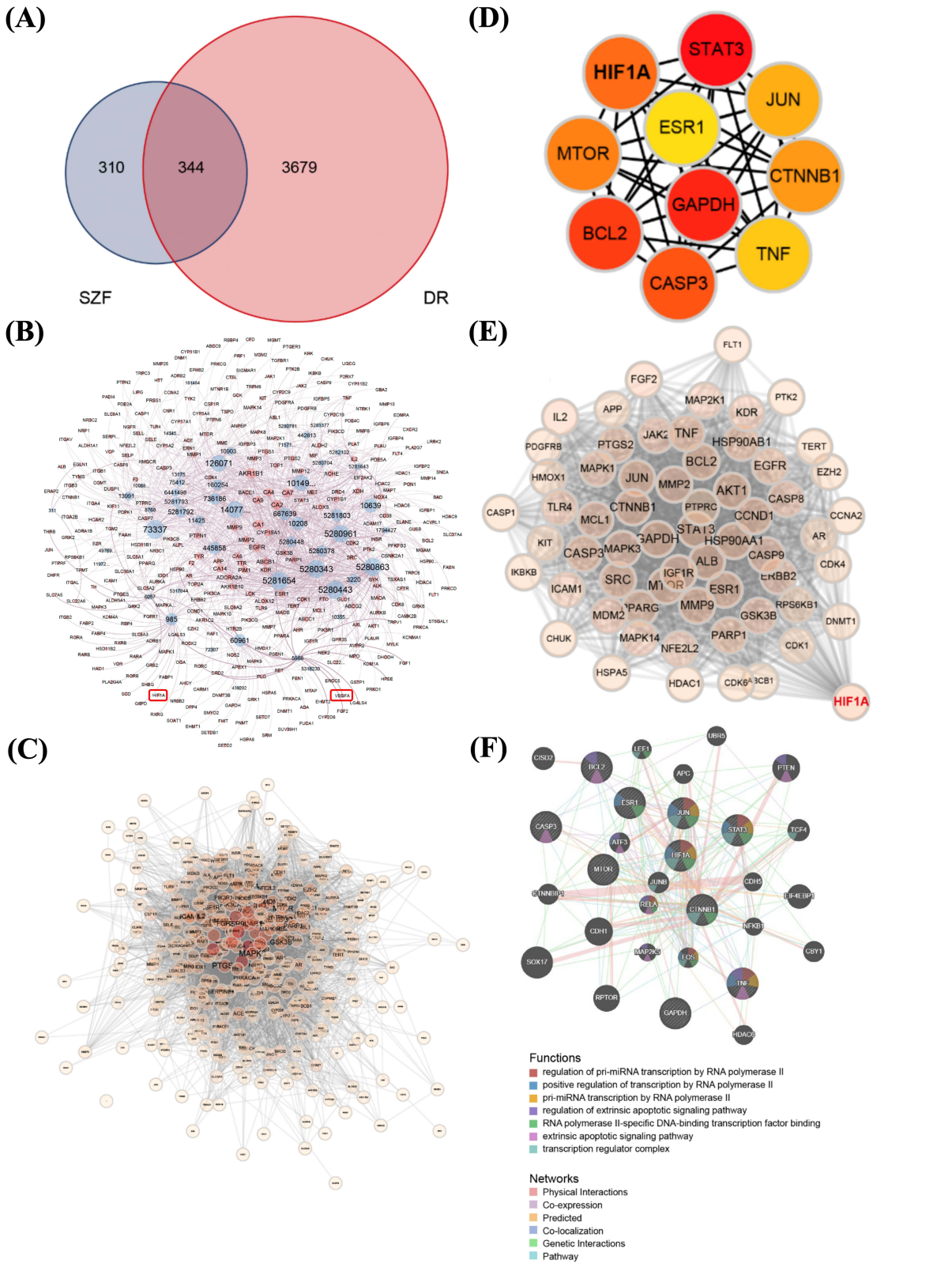

Figure 5 Regulating network of traditional Chinese medicine compound. (**A**) Venn diagram of disease and drug targets; (**B**) Component gene regulatory network. PPI and hub targets. (**C**) PPI network; (**D**) The top ten important targets of PPI discovered by Cytohuba plugin; (**E**) Module 1 discovered by MCODE plugin; (**F**) Use GeneMANIA to analyze Hub genes and their co expressed genes.

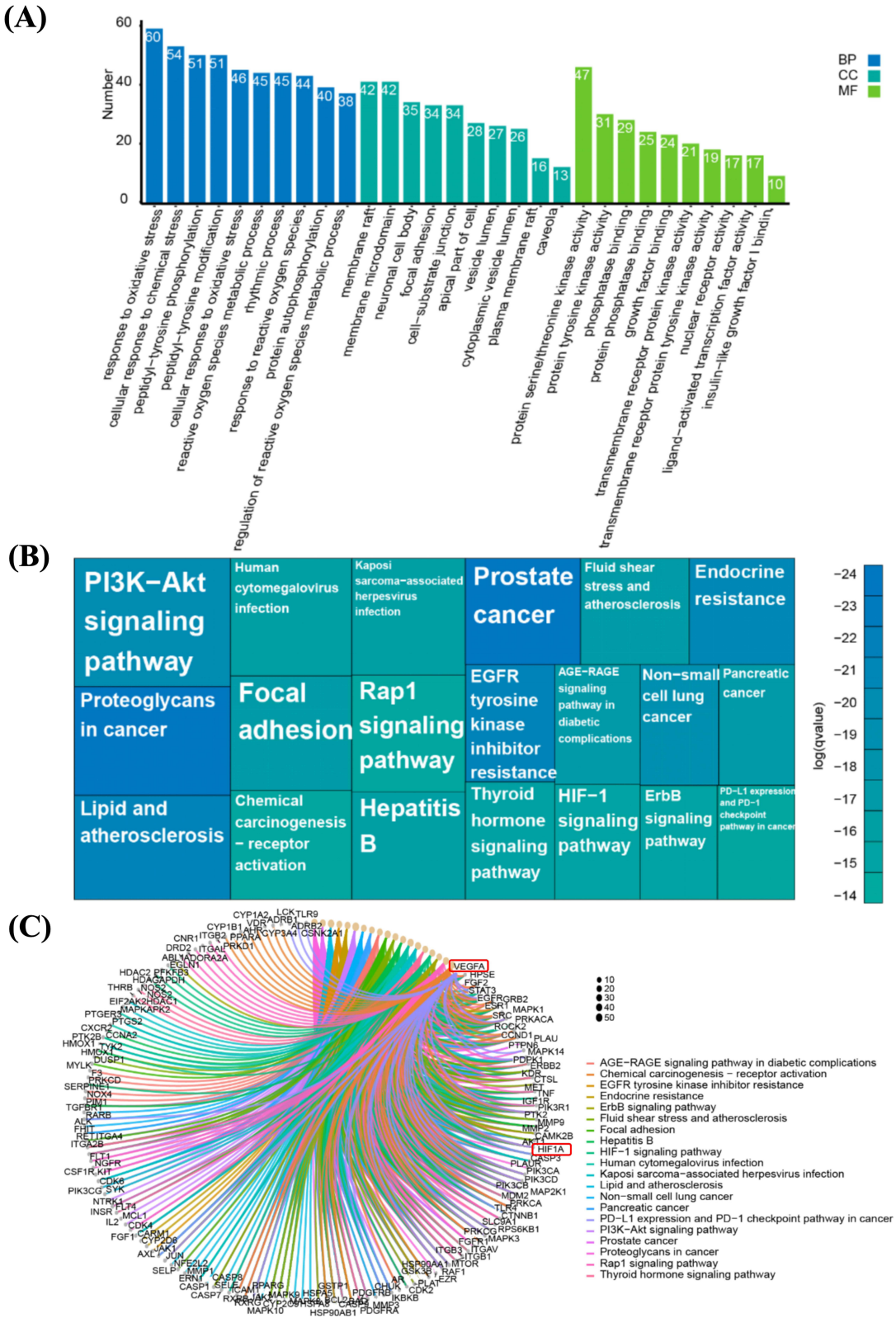

Figure 6 Functional enrichment analysis. (**A**) GO analysis results of DEGs. (**B**) KEGG analysis results of DEGs. (**C**) DEGs and pathway co expression network.

https://doi.org/10.2147/DDDT.S505055

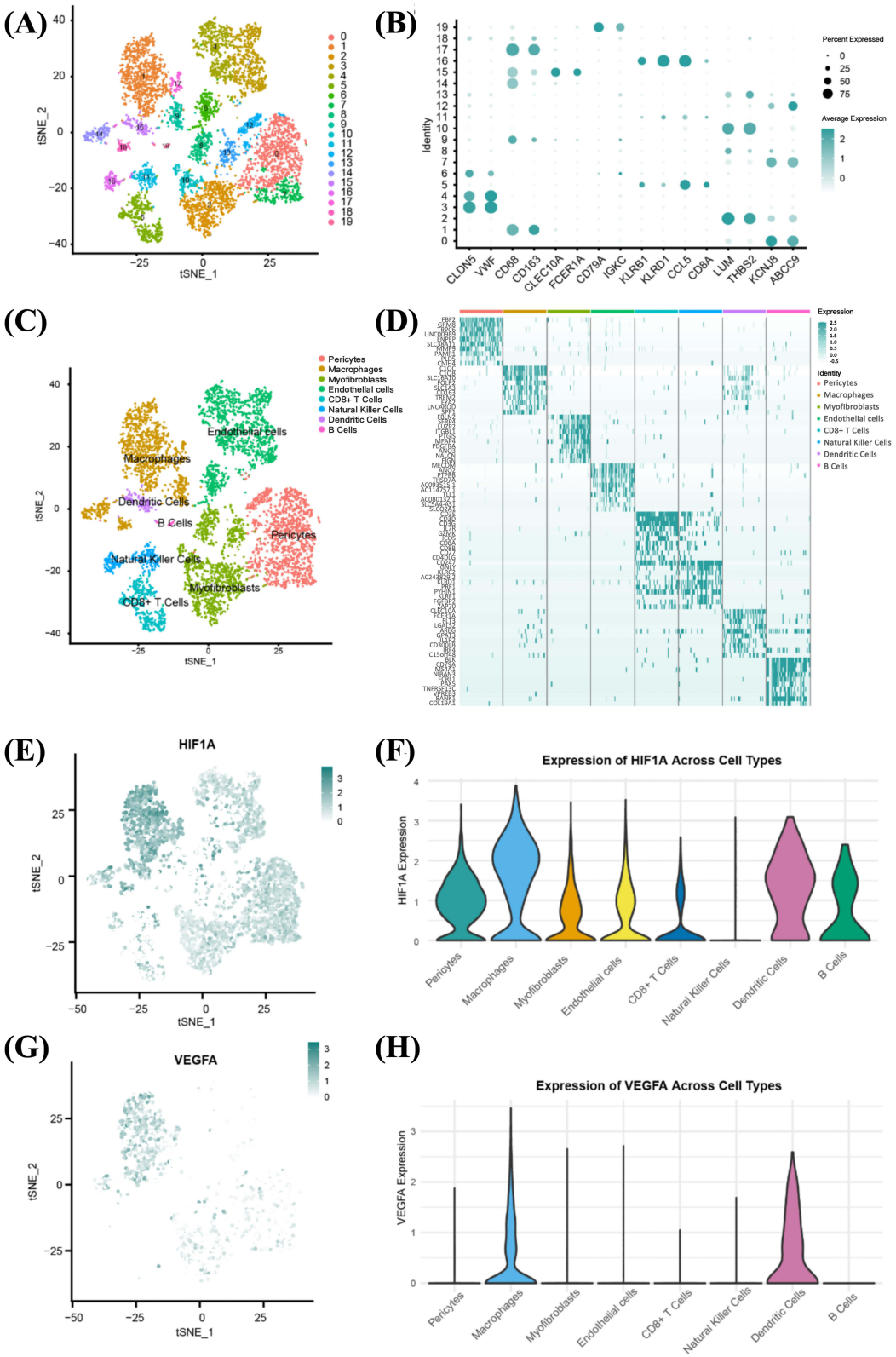

Figure 7 Single cell analysis results. (**A**) Unified manifold approximation and projection clustering into 20 clusters. (**B**) Dot plot of the most common biomarkers in different cells. (**C**) Manually annotate 20 clusters and ultimately determine 8 clusters. (**D**) Heatmap of TOP10 genes in different cells. (**E**) Distribution map of HIF1A on different cells; (**F**) The violin plot of HIF1A expression on different cells. (**G**) Distribution map of VEGF on different cells; (**H**) The violin plot of VEGF expression on different cells.

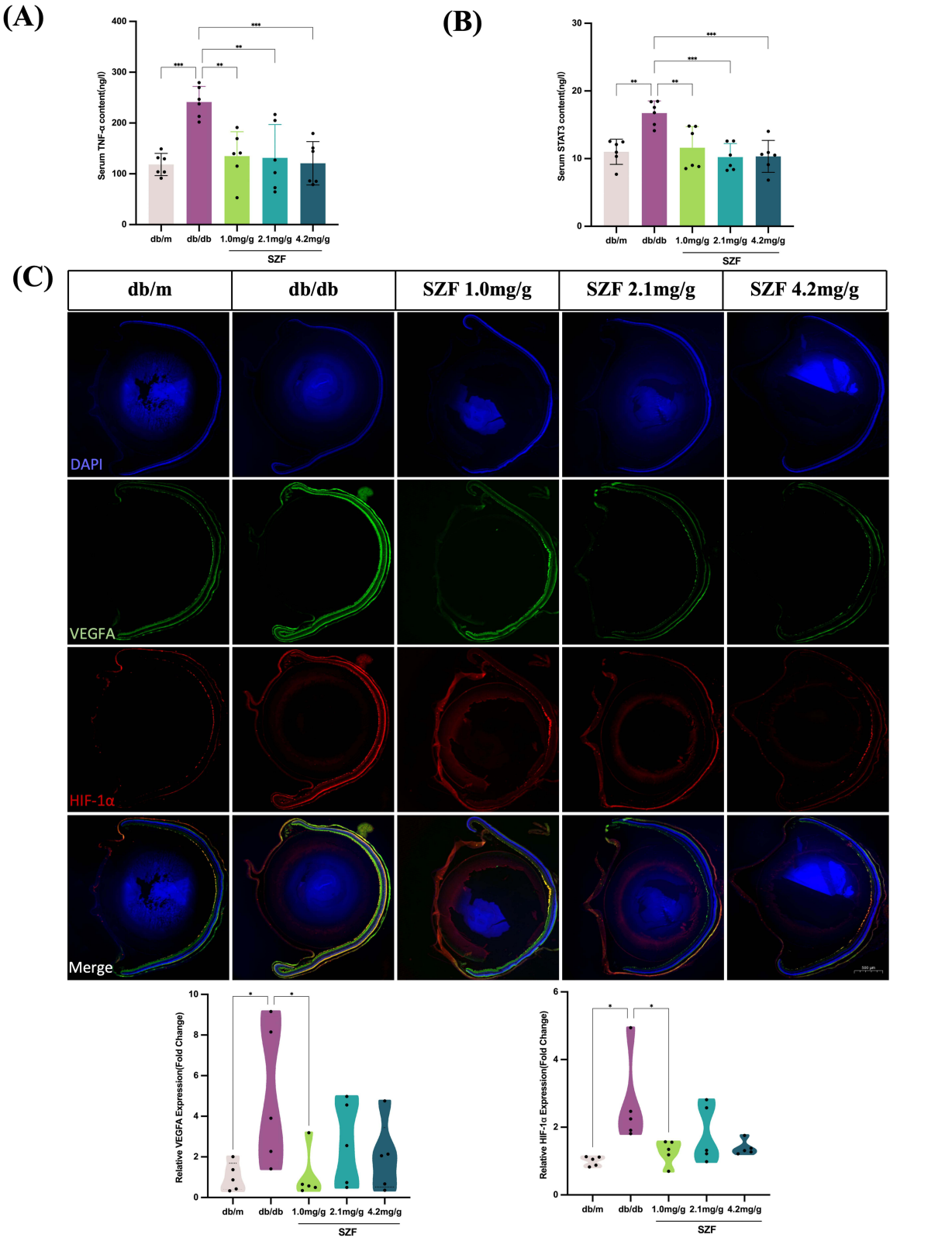

Figure 8 (**A**) Serum TNF α levels in five groups of mice. (**B**) Serum STAT3 levels in five groups of mice. (**C**) Representative images and normalized fluorescence intensity quantification from immunofluorescence analysis showed five groups of mice with co-localization of HIF-1α and VEGFA expression. Scale bar, 500 μm. n=5. *P<0.05, **P<0.01, ***P<0.001.

https://doi.org/10.2147/DDDT.S505055

SZF Delays DR Progression Through HIF-1α-VEGFA Pathway Regulation

Immunofluorescence assays were employed to evaluate the expression levels of HIF-1α and VEGFA. The results demonstrated that SZF treatment significantly decreased the levels of both HIF-1α and VEGFA. Furthermore, evidence suggested potential interaction between these proteins (Figure 8C).

Molecular Docking

Based on the established binding energy threshold criteria, quercetin and kaempferol exhibited the lowest binding energies with HIF-1α (−8.0 kcal/mol), significantly below the threshold of −7.5 kcal/mol, indicating their potential as strong binders with binding affinities superior to the positive control 2-ME2 (−6.68 kcal/mol). Apigenin also demonstrated strong binding affinity for VEGFA (−7.7 kcal/mol), comparable to the binding energies of known VEGFA inhibitors such as ranibizumab. The detailed binding mode analysis (Figure 9B–D) revealed multiple interactions between these compounds and key amino acid residues of the target proteins. The docking results from AutoDock Vina (Figure 9A) and CB-dock2 (Figure S2) are presented. These findings suggest that quercetin, kaempferol, and apigenin may serve as potential inhibitors of HIF-1α and VEGFA, warranting further experimental validation.

Discussion

This study systematically explored the mechanism of SZF in treating DR. Initially, we observed that SZF significantly improved multiple DR-related indicators in db/db mouse models, including fasting blood glucose levels, vascular leakage, structural changes in the inner nuclear layer (INL) and outer nuclear layer (ONL), and enhanced limb microcirculation. These findings prompted us to investigate its underlying mechanisms. First, we characterized the chemical composition of SZF using UPLC-Q-TOF-MS/MS and, combined with network pharmacology analysis, identified 344 potential therapeutic targets, highlighting SZF's advantage as a multi-component, multi-target therapeutic approach. To understand how these targets work in concert, we conducted PPI network analysis, which revealed that SZF simultaneously regulates multiple key biological processes, including apoptosis, inflammatory response, angiogenesis, hypoxic response, metabolic processes, and immune regulation. Notably, HIF-1α ranked fifth among the key targets, and since the retina is characterized by high energy and oxygen demands necessary for maintaining visual function, with the HIF-1 signaling pathway playing a crucial role in this process,[41,42] this led us to investigate the role of HIF-1α in TCM treatment of DR. Through pathway analysis, we found that thyroid hormone signaling pathway, HIF-1 signaling pathway, and VEGF signaling pathway are closely related to HIF-1α and VEGFA, and DR is closely associated with the regulation of retinal angiogenesis and leakage by HIF-1α and VEGF.[43,44] This prompted us to further verify through immunofluorescence experiments, which suggested that SZF may influence vascular permeability, potentially involving the HIF-1α-VEGFA pathway, though additional validations through Western blot or qPCR would be needed to confirm this mechanistic link. This discovery prompted us to further explore: in which cells do HIF-1α and VEGFA exert their effects? To answer this question, we analyzed single-cell RNA sequencing data from retinal samples of DR patients. Results showed that macrophages not only formed a unique cell subgroup but also exhibited high expression levels of both HIF-1α and VEGFA. This finding is significant because macrophage activation is considered a key factor in the occurrence and progression of DR.[45] Studies have shown that macrophages are the main source of intraocular VEGFA, promoting angiogenesis through the secretion of VEGF, TNF-α, and various interleukins.[46–48] Notably, HIF-1α activation is a key mechanism for VEGFA production in human macrophages.[49] According to Zhang et al's research,[50] under hyperglycemic conditions, oxidative stress and inflammatory responses synergistically activate macrophages, triggering this pathway. Based on this finding, we hypothesized that macrophage-mediated inflammatory response might be a crucial mechanism. To test this hypothesis, we examined inflammatory factor levels. Results showed that SZF significantly reduced TNF-α and STAT3 levels in the serum of DR model mice. Notably, these two factors ranked ninth and first respectively among key inflammatory factors in our earlier network pharmacology analysis, and extensive literature has confirmed their important roles in mediating DR inflammatory responses.[51] Combining the single-cell transcriptome analysis results, we propose a new perspective: TNF-α, STAT3, and HIF-1α/VEGFA may form a tight inflammation-hypoxia-vascular regulation network, jointly participating in the pathological activation of macrophages. This led us to consider: which components in SZF play key roles in this network? Preliminary molecular docking analysis suggested that quercetin and apigenin could potentially interact with HIF-1α and

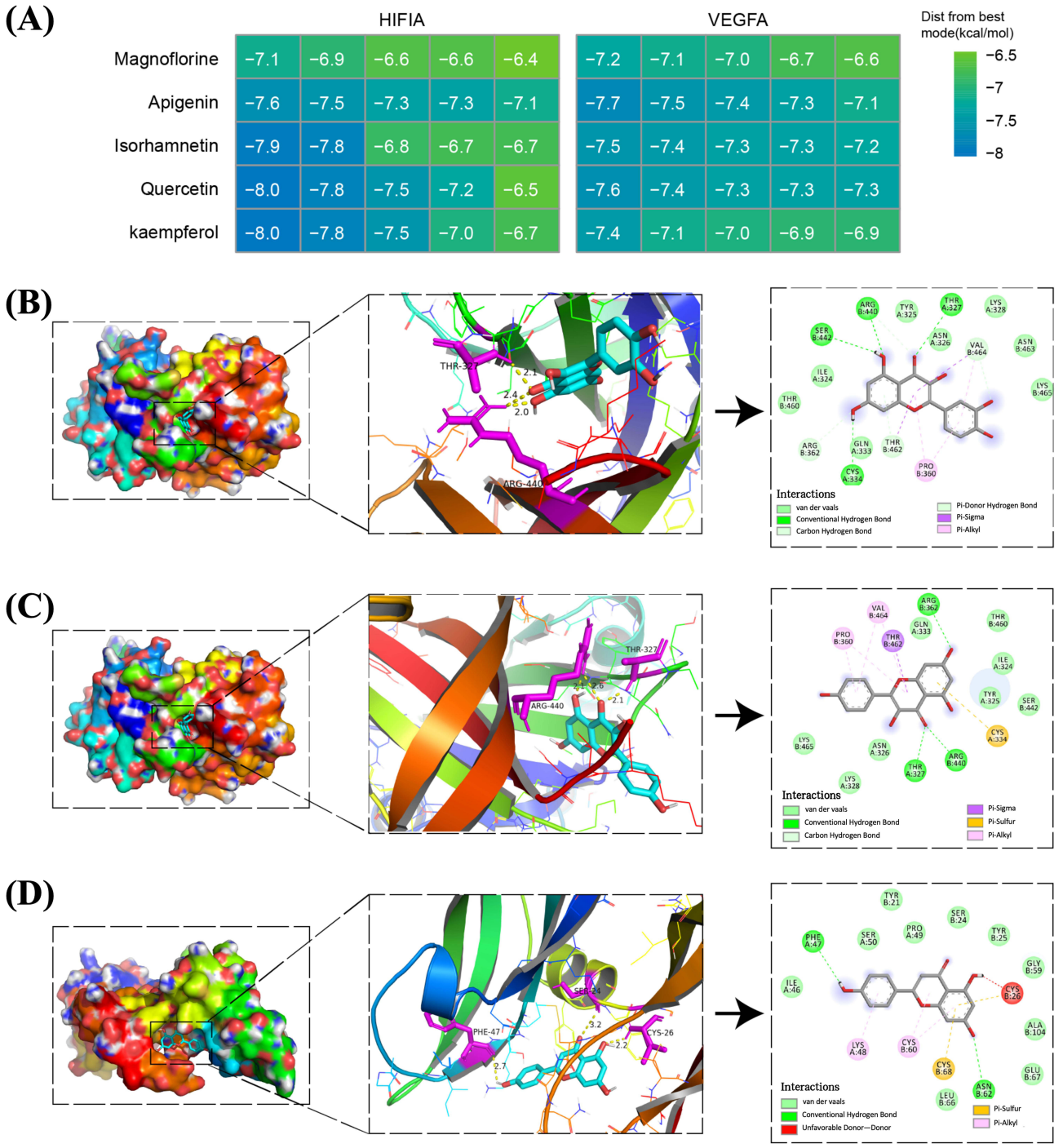

Figure 9 Molecular docking results. (**A**) Heatmap showing five docking analyses of 5 key active ingredients from SZF with VEGFA and HIF1A targets using AutoDock Vina. (**B**) Quercetin and HIF1A binding mode. (**C**) Kaempferol and HIF1A binding mode. (**D**) Apigenin binding mode with VEGFA. The middle dashed line represents hydrogen bonds, and the numerical value is the bond length.

VEGFA, although these computational predictions require experimental validation and comparison with established ligands to determine their biological significance. This finding is particularly significant because these two compounds have been proven to have notable antioxidant and anti-inflammatory properties.[52,53] Based on our preliminary findings, we propose a possible mechanism for SZF's effects: its components quercetin and apigenin might contribute to alleviating DR symptoms, possibly through interactions with the HIF-1α-VEGFA pathway in macrophages, which could help reduce retinal leakage, though further functional studies are needed to validate this hypothesis.

https://doi.org/10.2147/DDDT.S505055

These mechanistic insights not only clarify the molecular basis of SZF in treating DR but also highlight its potential as a new treatment option for DR. Compared with other reported TCM compound studies, this research has several advantages: First, we adopted a systematic research strategy from chemical composition characterization to network pharmacology analysis and single-cell sequencing data mining, enabling a more comprehensive understanding of the compound's mechanism. Second, we discovered for the first time the key role of macrophages in SZF's treatment of DR and elucidated the regulatory mechanism of the HIF-1α-VEGFA pathway, providing new therapeutic targets for TCM compounds in treating DR. Furthermore, we validated SZF's safety through a 12-week sub-acute toxicity assessment. Sub-acute toxicity studies are crucial for evaluating the safety of TCM preparations, which is essential for guiding clinical applications.[54] Such studies can reveal potential toxic reactions and provide scientific basis for determining safe dosage ranges. In this study, through 12 weeks of sub-acute toxicity assessment, we systematically observed SZF's effects on db/db mice's general condition (food and water intake), liver function (ALT, AST), and kidney function (CREA, UREA, BUN/CREA). Results confirmed that SZF has good safety characteristics within the therapeutic dose range, with no obvious toxic reactions observed. These findings not only support SZF's therapeutic efficacy but also provide important experimental evidence for its safe clinical application.

However, this study has some limitations: (1) molecular docking results need further experimental verification; (2) the finding of macrophages as HIF-1α/VEGFA target cells needs more in vitro and in vivo experimental support; (3) the lack of positive control groups in our experiments may limit the interpretation of the therapeutic effects. These issues will be the focus of our future research.

Conclusion

In the db/db mouse model of DR, SZF showed promising potential in potentially alleviating DR progression. Our preliminary findings suggest that SZF may enhance the structural integrity of retinal layers, particularly INL and ONL, and reduce retinal vascular leakage. Immunofluorescence observations suggest a possible association with HIF-1α and VEGFA expression, though additional validation through Western blot or qPCR is needed to support these mechanistic implications. Computational analyses hint that compounds such as Quercetin and Apigenin in SZF might theoretically interact with these pathway components, but these predictions require experimental confirmation. The integration of chemical characterization, network pharmacology, and single-cell sequencing provides a framework for examining potential mechanisms, though the exact pathways remain to be elucidated. While our data points to macrophages as potential mediators, further functional studies are essential to verify this hypothesis and identify the specific bioactive compounds responsible for the observed effects.

Abbreviations

DR, Diabetic retinopathy; FP, Fundus photography; FFA, Fundus fluorescein angiography; OCT, Optical coherence tomography; H&E, Hematoxylin and eosin; NP, Network pharmacology; UPLC-Q-TOF-MS/MS, Ultra Performance Liquid Chromatography-Quadrupole Time-of-Flight Mass Spectrometry/Mass Spectrometry; ADA, The American Diabetes Association; PEDF, Pigment epithelium derived factor; SST, Somatostatin; PACAP, Pituitary adenylate cyclase activating polypeptide; GLP-1, Glucagon like peptide-1; BDNF, Brain-derived neurotrophic factor; NGF, Nerve growth factor; SGLT2, Sodium-Glucose Cotransporter-2; PPAR-α, Peroxisome Proliferator-Activated Receptor alpha; TCM, Traditional Chinese medicine; PPI, Protein-protein interaction; UMAP, Unified Manifold Approximation and Projection; SPF, Specific pathogen-free; INL, The Inner Nuclear Layer; ONL, The Outer Nuclear Layer; GCL, The Ganglion Cell Layer; PBS, Phosphate buffered saline; BSA, Bovine serum albumin; VEGFA, Vascular Endothelial Growth Factor A; HIF-1α, Hypoxia-Inducible Factor 1-alpha; TSA, Tyramide Signal Amplification; TBST, Tris-Buffered Saline with Tween 20; TNF-α, Tumor necrosis factor-alpha; STAT3, Signal Transducer and Activator of Transcription 3; DEGs, Differentially expressed genes; GAPDH, Glyceraldehyde 3-phosphate dehydrogenase; BCL2, B-cell lymphoma 2; CASP3, Caspase-3; MTOR, Mammalian target of rapamycin; CTNNB1, Catenin Beta 1; JUN, Jun proto-oncogene; ESR1, Estrogen Receptor 1; RNA, Ribonucleic Acid.

Data Sharing Statement

The data associated with this study can be obtained from the corresponding author upon reasonable request.

Ethics Statement

The data used in the "Analysis of single-cell RNA sequencing data and identification of DR related genes" section of this study were obtained from publicly accessible datasets. The data used in this investigation were obtained from publicly accessible datasets with complete informed consent. China's scientific and technological authorities released the "Measures for Ethical Review of Life Science and Medical Research Involving Human Beings" in 2023. According to clause 32 of the Measures for Ethical Review, ethical review can be exempted if research is conducted using legally obtained public data.

Consent for Publication

This submission has been approved for publication by all authors.

Acknowledgments

The graphical abstract was created using FrgDraw 2.0 (Authorization ID: WYTOUddd4d).

Funding

This work was supported by the Innovation Team and Talents Cultivation Program of National Administration of Traditional Chinese Medicine [grant number ZYYCXTD-D-202001]; the Noncommunicable Chronic Diseases-National Science and Technology Major Project [2023ZD0509305]; the Clinical Research Fund of the Central High-level Hospital of Traditional Chinese Medicine [grant number HLCMHPP2023084]; the Scientific and Technological Innovation Project of China Academy of Chinese Medical Sciences [grant number CI2023C024YL]; the Young Elite Scientists Sponsorship Program by CACM [grant number CACM-2023-QNRC2-A08]; and the Beijing Natural Science Foundation [grant number 7244497].

Disclosure

The authors report no conflicts of interest in this work.

References

1. Solomon SD, Chew E, Duh EJ, et al. Diabetic retinopathy: a position statement by the American Diabetes Association. *Diabetes Care*. 2017;40(3):412–418. doi:10.2337/dc16-2641
2. Teo ZL, Tham YC, Yu M, et al. Global prevalence of diabetic retinopathy and projection of burden through 2045: systematic review and meta-analysis. *Ophthalmology*. 2021;128(11):1580–1591. doi:10.1016/j.ophtha.2021.04.027
3. GBD 2019 Blindness and Vision Impairment Collaborators, Vision Loss Expert Group of the Global Burden of Disease Study. Causes of blindness and vision impairment in 2020 and trends over 30 years, and prevalence of avoidable blindness in relation to VISION 2020: the Right to sight: an analysis for the global burden of disease study. *Lancet Glob Health*. 2021;9(2):e144–e160. doi:10.1016/s2214-109x(20)30489-7
4. Kowluru RA. Cross talks between oxidative stress, inflammation and epigenetics in diabetic retinopathy. *Cells*. 2023;12(2):300. doi:10.3390/cells12020300
5. Lin Z, Deng A, Hou N, Gao L, Zhi X. Advances in targeted retinal photocoagulation in the treatment of diabetic retinopathy. *Front Endocrinol*. 2023;14:1108394. doi:10.3389/fendo.2023.1108394
6. Sood A, Baishnab S, Gautam I, et al. Exploring various novel diagnostic and therapeutic approaches in treating diabetic retinopathy. *Inflammopharmacology*. 2023;31(2):773–786. doi:10.1007/s10787-023-01143-x
7. Fong DS, Girach A, Boney A. Visual side effects of successful scatter laser photocoagulation surgery for proliferative diabetic retinopathy: a literature review. *Retina*. 2007;27(7):816–824. doi:10.1097/IAE.0b013e318042d32c
8. Leite EB, Mota MC, de Abreu JR, Cunha-Vaz JG. Effect of calcium dobesilate on the blood-retinal barrier in early diabetic retinopathy. *Int Ophthalmol*. 1990;14(2):81–88. doi:10.1007/bf00154206
9. Ribeiro ML, Seres AI, Carneiro AM, et al. Effect of calcium dobesilate on progression of early diabetic retinopathy: a randomised double-blind study. *Graefes Arch Clin Exp Ophthalmol*. 2006;244(12):1591–1600. doi:10.1007/s00417-006-0318-2
10. Simó R, Hernández C. Novel approaches for treating diabetic retinopathy based on recent pathogenic evidence. *Prog Retin Eye Res*. 2015;48:160–180. doi:10.1016/j.preteyeres.2015.04.003
11. Chaturvedi N, Porta M, Klein R, et al. Effect of candesartan on prevention (DIRECT-Prevent 1) and progression (DIRECT-Protect 1) of retinopathy in type 1 diabetes: randomised, placebo-controlled trials. *Lancet*. 2008;372(9647):1394–1402. doi:10.1016/s0140-6736(08)61412-9
12. Rodrigues EB, Farah ME, Maia M, et al. Therapeutic monoclonal antibodies in ophthalmology. *Prog Retin Eye Res*. 2009;28(2):117–144. doi:10.1016/j.preteyeres.2008.11.005
13. Grunwald JE, Daniel E, Huang J, et al. Risk of geographic atrophy in the comparison of age-related macular degeneration treatments trials. *Ophthalmology*. 2014;121(1):150–161. doi:10.1016/j.ophtha.2013.08.015
14. Zhou J, Chen B. Retinal cell damage in diabetic retinopathy. *Cells*. 2023;12(9):1342. doi:10.3390/cells12091342

15. Cox JT, Eliott D, Sobrin L. Inflammatory complications of intravitreal anti-VEGF injections. *J Clin Med*. 2021;10(5):981. doi:10.3390/jcm10050981
16. Simó R, Hernández C. New insights into treating early and advanced stage diabetic retinopathy. *Int J Mol Sci*. 2022;23(15):8513. doi:10.3390/ijms23158513
17. Zhang YH. Di Dang Tang in the treatment of insulin resistance in type 2 diabetes–report of 37 cases. *Zhongguo Zhong Xi Yi Jie He Za Zhi*. 2008;28(2):161–162.
18. Sun HH, Chai XL, Li HL, et al. Fufang Xueshuantong alleviates diabetic retinopathy by activating the PPAR signalling pathway and complement and coagulation cascades. *J Ethnopharmacol*. 2021;265:113324. doi:10.1016/j.jep.2020.113324
19. Jian W, Yu S, Tang M, Duan H, Huang J. A combination of the main constituents of Fufang Xueshuantong capsules shows protective effects against streptozotocin-induced retinal lesions in rats. *J Ethnopharmacol*. 2016;182:50–56. doi:10.1016/j.jep.2015.11.021
20. Ding Y, Yuan S, Liu X, et al. Protective effects of astragaloside IV on db/db mice with diabetic retinopathy. *PLoS One*. 2014;9(11):e112207. doi:10.1371/journal.pone.0112207
21. Jin Q, Hao XF, Xie LK, et al. A network pharmacology to explore the mechanism of astragalus membranaceus in the treatment of diabetic retinopathy. *Evid Based Complement Alternat Med*. 2020;2020:8878569. doi:10.1155/2020/8878569
22. Chai GR, Liu S, Yang HW, Chen XL. Quercetin protects against diabetic retinopathy in rats by inducing heme oxygenase-1 expression. *Neural Regen Res*. 2021;16(7):1344–1350. doi:10.4103/1673-5374.301027
23. Albalawi FE, Alsharif I, Moawadh MS, et al. Immunomodulatory effects of Kaempferol on microglial and Macrophage cells during the progression of diabetic retinopathy. *Int Immunopharmacol*. 2024;133:112021. doi:10.1016/j.intimp.2024.112021
24. Mei X, Zhou L, Zhang T, Lu B, Sheng Y, Ji L. Chlorogenic acid attenuates diabetic retinopathy by reducing VEGF expression and inhibiting VEGF-mediated retinal neoangiogenesis. *Vascul Pharmacol*. 2018;101:29–37. doi:10.1016/j.vph.2017.11.002
25. Ouyang H, Du A, Zhou L, et al. Chlorogenic acid improves diabetic retinopathy by alleviating blood-retinal-barrier dysfunction via inducing Nrf2 activation. *Phytother Res*. 2022;36(3):1386–1401. doi:10.1002/ptr.7401
26. Ouyang H, Xie Y, Du A, et al. Chlorogenic acid ameliorates non-proliferative diabetic retinopathy via alleviating retinal inflammation through targeting TNFR1 in retinal endothelial cells. *Int Immunopharmacol*. 2024;141:112929. doi:10.1016/j.intimp.2024.112929
27. Wu W, Xie Z, Zhang Q, et al. Hyperoside Ameliorates diabetic retinopathy via anti-oxidation, inhibiting cell damage and apoptosis induced by high glucose. *Front Pharmacol*. 2020;11:797. doi:10.3389/fphar.2020.00797
28. Szklarczyk D, Gable AL, Nastou KC, et al. Correction to 'the STRING database in 2021: customizable protein-protein networks, and functional characterization of user-uploaded gene/measurement sets'. *Nucleic Acids Res*. 2021;49(18):10800. doi:10.1093/nar/gkab835
29. Chin CH, Chen SH, Wu HH, Ho CW, Ko MT, Lin CY. cytoHubba: identifying hub objects and sub-networks from complex interactome. *BMC Syst Biol*. 2014;8(Suppl 4):S11. doi:10.1186/1752-0509-8-s4-s11
30. Bader GD, Hogue CW. An automated method for finding molecular complexes in large protein interaction networks. *BMC Bioinformatics*. 2003;4:2. doi:10.1186/1471-2105-4-2
31. Franz M, Rodriguez H, Lopes C, et al. GeneMANIA update 2018. *Nucleic Acids Res*. 2018;46(W1):W60–w64. doi:10.1093/nar/gky311
32. Wang A, Li Z, Sun Z, Liu Y, Zhang D, Ma X. Potential mechanisms between HF and COPD: new insights from bioinformatics. *Curr Probl Cardiol*. 2023;48(3):101539. doi:10.1016/j.cpcardiol.2022.101539
33. Chen H, Guo J, Zhao X, et al. Retrospective analysis of the overt proteinuria diabetic kidney disease in the treatment of modified Shenzhuo formula for 2 years. *Medicine*. 2017;96(12):e6349. doi:10.1097/md.0000000000006349
34. Zhao XM, Zhang Y, He XH, et al. Chinese herbal medicine Shenzhuo Formula treatment in patients with macroalbuminuria secondary to diabetic kidney disease: study protocol for a randomized controlled trial. *Trials*. 2018;19(1):200. doi:10.1186/s13063-018-2573-z
35. Xu S, Bian R, Chen X. *Methodology of Pharmacological Experiment*. People's Health Publishing House. 2022.
36. Liu Y, Yang X, Gan J, Chen S, Xiao ZX, Cao Y. CB-Dock2: improved protein-ligand blind docking by integrating cavity detection, docking and homologous template fitting. *Nucleic Acids Res*. 2022;50(W1):W159–w164. doi:10.1093/nar/gkac394
37. Reda D, Elfiky AA, Elnagdy M, Khalil MM. Molecular docking and molecular dynamics of hypoxia-inducible factor (HIF-1alpha): towards potential inhibitors. *J Biomol Struct Dyn*. 2024;1–20. doi:10.1080/07391102.2024.2425839
38. Platania CB, Di Paola L, Leggio GM, et al. Molecular features of interaction between VEGFA and anti-angiogenic drugs used in retinal diseases: a computational approach. *Front Pharmacol*. 2015;6:248. doi:10.3389/fphar.2015.00248
39. Liang D, Qi Y, Liu L, et al. Jin-Gui-Shen-Qi Wan ameliorates diabetic retinopathy by inhibiting apoptosis of retinal ganglion cells through the Akt/HIF-1α pathway. *Chin Med*. 2023;18(1):130. doi:10.1186/s13020-023-00840-7
40. Fieberg JR, Vitense K, Johnson DH. Resampling-based methods for biologists. *PeerJ*. 2020;8:e9089. doi:10.7717/peerj.9089
41. Yu DY, Cringle SJ, Yu PK, et al. Retinal capillary perfusion: spatial and temporal heterogeneity. *Prog Retin Eye Res*. 2019;70:23–54. doi:10.1016/j.preteyeres.2019.01.001
42. Huang R, Xu Y, Lu X, et al. Melatonin protects inner retinal neurons of newborn mice after hypoxia-ischemia. *J Pineal Res*. 2021;71(1):e12716. doi:10.1111/jpi.12716
43. Wu J, Ke X, Wang W, et al. Aloe-emodin suppresses hypoxia-induced retinal angiogenesis via inhibition of HIF-1α/VEGF pathway. *Int J Biol Sci*. 2016;12(11):1363–1371. doi:10.7150/ijbs.16334
44. Han N, Xu H, Yu N, Wu Y, Yu L. MiR-203a-3p inhibits retinal angiogenesis and alleviates proliferative diabetic retinopathy in oxygen-induced retinopathy (OIR) rat model via targeting VEGFA and HIF-1α. *Clin Exp Pharmacol Physiol*. 2020;47(1):85–94. doi:10.1111/1440-1681.13163
45. Zhang Y, Zhou A. Macrophage activation contributes to diabetic retinopathy. *J Mol Med*. 2024;102(5):585–597. doi:10.1007/s00109-024-02437-5
46. Apte RS. Regulation of angiogenesis by macrophages. *Adv Exp Med Biol*. 2010;664:15–19. doi:10.1007/978-1-4419-1399-9_2
47. Rangasamy S, McGuire PG, Franco Nitta C, Monickaraj F, Oruganti SR, Das A. Chemokine mediated monocyte trafficking into the retina: role of inflammation in alteration of the blood-retinal barrier in diabetic retinopathy. *PLoS One*. 2014;9(10):e108508. doi:10.1371/journal.pone.0108508
48. Kovoor E, Chauhan SK, Hajrasouliha A. Role of inflammatory cells in pathophysiology and management of diabetic retinopathy. *Surv Ophthalmol*. 2022;67(6):1563–1573. doi:10.1016/j.survophthal.2022.07.008
49. Eubank TD, Roda JM, Liu H, O'Neil T, Marsh CB. Opposing roles for HIF-1α and HIF-2α in the regulation of angiogenesis by mononuclear phagocytes. *Blood*. 2011;117(1):323–332. doi:10.1182/blood-2010-01-261792

50. Zhang Q, Cunha APD, Li S, et al. IL-27 regulates HIF-1α-mediated VEGFA response in macrophages of diabetic retinopathy patients and healthy individuals. *Cytokine*. 2019;113:238–247. doi:10.1016/j.cyto.2018.07.011
51. Tang L, Xu GT, Zhang JF. Inflammation in diabetic retinopathy: possible roles in pathogenesis and potential implications for therapy. *Neural Regen Res*. 2023;18(5):976–982. doi:10.4103/1673-5374.355743
52. Alam W, Rocca C, Khan H, et al. Current status and future perspectives on therapeutic potential of apigenin: focus on metabolic-syndrome-dependent organ dysfunction. *Antioxidants*. 2021;10(10). doi:10.3390/antiox10101643
53. Hosseini A, Razavi BM, Banach M, Hosseinzadeh H. Quercetin and metabolic syndrome: a review. *Phytother Res*. 2021;35(10):5352–5364. doi:10.1002/ptr.7144
54. Girigoswami A, Ghosh MM, Girigoswami K. World scenario of earthworms' prowess as a remedy to a spectrum of diseases–a glimpse on related nanoformulations. *Tradit Med Res*. 2025;10(4):23. doi:10.53388/tmr20240822001